CrystEngComm

PAPER

View Article Online
View Journal | View Issue

On the crystallization of Ta_2O_5 nanotubes: structural and local atomic properties investigated by EXAFS and XRD†

Cite this: *CrystEngComm*, 2014, **16**, 797

Renato V. Gonçalves,*[a] Pedro Migowski,*[b] Heberton Wender,[c] Adriano F. Feil,[d] Maximiliano J. M. Zapata,[b] Sherdil Khan,[b] Fabiano Bernardi,[b] Gustavo M. Azevedo[b] and Sergio R. Teixeira[b]

Metal oxide nanotubes (NTs) semiconductors prepared by anodization are promising materials due to their expected unique optical and electric properties. However, most of the work reported to date did not find photoelectrochemical devices with higher efficiency than those assembled with nanoparticles. Moreover, this behavior is due to the difficulty of having non-defective crystalline structures and the disruption of the tubular shape during thermal treatment while trying to reduce oxygen vacancies. This work describes in detail the local atomic configuration, surface area and morphology properties of Ta_2O_5 NTs prepared by anodization as a function of the temperature and the crystallization time by using X-ray diffraction (XRD) and X-ray absorption spectroscopy (XAS). The crystallization process of adhered and freestanding Ta_2O_5 NTs is discussed. Adhered NTs crystallized at 550 °C due to the oxidation of the Ta metal during annealing in the air atmosphere and not the NT array itself. Freestanding Ta_2O_5 NTs crystallized after annealing at 800 °C. Rietveld refinements were performed to investigate the effects of the temperature and the annealing time on the grain size and microstrain and obtain information about Ta–O interatomic distances. The local structure of amorphous and crystalline Ta_2O_5 NTs was investigated with EXAFS. Low coordination numbers were found in the as-anodized samples as well as the samples annealed for 30 min at 800 °C. The coordination number increased when annealing was performed above 800 °C or when the annealing time was longer than 30 min. Moreover, the decrease of defects was followed by an increase in the crystal size and collapse of the tubular shape due to the increase in internal stress generated by the increase in the crystallinity of the tubes and the orthorhombic Ta_2O_5 crystal size.

Received 8th October 2013,
Accepted 31st October 2013

DOI: 10.1039/c3ce42043d

www.rsc.org/crystengcomm

1 Introduction

One-dimensional (1D) semiconductor nanostructures such as nanotubes (NTs), nanowires and nanorods are promising materials for next-generation electronic, photoelectronic, electrochemical and photoelectrochemical devices.[1] Most applications for 1D nanomaterials are related to their unique optical[2–4] and electrical properties.[5] Moreover, these properties can be tuned not only by choosing the chemical composition of the nanostructure but also by tailoring its specific geometry.[6]

For example, TiO_2 NTs prepared by anodization are promising alternatives for technological applications such as photocatalysis[7] and photoelectrochemical cells (Grätzel solar cells).[8–10] The main advantages of using such materials seem to be due to directed charge transport, high light-harvesting and slower recombination rates through the length of the aligned and vertically oriented NTs.[11]

Synthesis of anodic NTs semiconductors was first reported by Gong *et al.* in 2001[12] and is one of the easiest approaches for preparing 1D materials. Due to the simplicity and versatility of the process, several authors have obtained vertically aligned oxide NTs with this methodology, including a wide range of materials such as Ta_2O_5,[13,14] Fe_2O_3,[15] ZrO_2[16] and TiO_2.[17–19]

Recently, some reports have suggested that the morphology of anodic semiconductor oxide NTs offers unique advantages providing a direct and rapid pathway for transporting electrons, which increases the electron lifetimes in semiconductor

[a] *Laboratory of Nanomaterials & Catalysis, University of São Paulo-Institute of Chemistry, Av. Professor Lineu Prestes, 748 São Paulo, SP, Brazil. E-mail: rsvg12@iq.usp.br*
[b] *Institute of Physics, IF-UFRGS, Av. Bento Gonçalves 9500, P.O. Box 15051, 91501-970, Porto Alegre, RS, Brazil. E-mail: pedro.migowski@ufrgs.br*
[c] *Institute of Physics, INFI-UFMS, Cidade Universitária, P.O. Box 549, CEP 79070-900, Campo Grande, MS, Brazil*
[d] *Institute of Physics, PUCRS, Av. Ipiranga 6681, Porto Alegre, RS, Brazil*
† Electronic supplementary information (ESI) available. See DOI: 10.1039/c3ce42043d

electrodes.[10,20–23] However, the electron transport constants of TiO_2 NTs and interconnected nanoparticles (NPs) in dye-sensitized solar cells (DSSCs) lies at the same time scale.[24] There is no plausible explanation for why electron transport is not significantly faster in NTs than in the NPs oxide electrodes,[11] since the recombination times in the nanotubular semiconductor structure is approximately 1 order of time higher than in NP films.[24] A very interesting work published by Richter and Schmuttenmaer provided insights that try to explain the slow charge diffusion through TiO_2 NTs.[25] Richter and Schmuttenmaer observed with time-resolved terahertz spectroscopy that the trapping sites in TiO_2 NTs have an exciton-like character due to the Ti^{3+} sites. If these defects are decreased, then the conductivity in TiO_2 NTs can be increased. The Ti^{3+} sites may be due to the presence of F^- impurities and/or oxygen vacancies from the anodization process.

One way to remove the vacancies and impurities is to anneal the samples in oxygen-rich environments.[26,27] In an ideal scenario, the annealing would also increase the crystallinity of the semiconductor, and increase its conductivity. However, in practice, long times and high temperatures are needed for crystallization in conventional muffle furnaces, which causes the tubular structure to collapse.[20,23,28]

Usually, the NTs are prepared by anodizing pure metal foils, and the semiconductor array stands over the metal foil. Crystallization of the NTs over the metal substrate drives the premature growth of crystal phases and/or grains, which induces morphological changes on the 1D structure.[20,23,28–31] Moreover, almost all studies reported to date dealt with the crystallization behavior of TiO_2 NTs obtained by anodization in fluoride electrolytes. Thus, we should investigate how NT arrays from another semiconductor oxide crystallize under various annealing temperatures, since we might learn how to control the crystallization of TiO_2 NTs for photoelectrochemical applications. In particular, there are no detailed reports on the crystallization behavior of high-aspect-ratio Ta_2O_5 nanotube arrays obtained by anodization of tantalum foils in sulfuric acid, hydrofluoric acid and water electrolyte.[13,14,32,33]

In a previous work, we developed an easy method for fabricating adhered and freestanding Ta_2O_5 NTs simply by controlling the anodization parameters.[34] With this methodology, we can investigate the crystallization behavior of Ta_2O_5 NTs adhered on the Ta substrate and freestanding Ta_2O_5 NTs. Herein, the structural properties, local atomic configuration, surface area and morphology properties of Ta_2O_5 NTs and their dependence on the temperature and the annealing time were studied in detail with X-ray diffraction (XRD) and X-ray absorption spectroscopy (XAS).

2 Experimental

2.1 Materials

Tantalum foil (99.99% purity, Goodfellow), sulfuric acid (98%, Synth), hydrofluoric acid (40%, Nuclear), ethanol (EtOH, 95%, Fmaia) and acetone (Synth) were used as received.

2.2 Anodization process

The tantalum foils used in the anodization experiments were cleaned ultrasonically in an acetone bath for 20 min, rinsed with distilled water (DI) and further dried in a nitrogen stream. Anodization was performed in a H_2SO_4 + 1 vol% HF + 4 vol% DI electrolyte at 20 °C and 50 °C, as reported in our previous work.[34] The samples were annealed in a muffle furnace under atmospheric air at different temperatures, with a heating rate of 5 °C min^{-1}.

2.3 Microscopy analysis and crystalline structure

The morphologies of the Ta_2O_5 NTs were characterized with field emission scanning electron microscopy (FESEM) using an FEI Inspect F50 operated at 10–30 kV. X-ray diffraction (XRD) of the adhered and freestanding Ta_2O_5 NTs was recorded with a Philips X'PERT diffractometer with Cu K_α radiation (λ = 1.54 Å) at 2θ = 5–100° with a 0.02° step size and a measuring time of 5 s per step. The crystal structure of the Ta_2O_5 NTs after thermal treatment for Rietveld profile refinement was performed with Fullprof software.[35] The degree of crystallinity (X_C) of the NTs, annealed at different temperatures, was determined from the ratio of the integral intensity of the crystalline contribution to the total intensity.[36]

2.4 Specific surface area

The specific surface area (S_{BET}) was measured according to the Brunauer–Emmett–Teller method (BET) using nitrogen absorption isotherms obtained in a Micromeritics TriStar II 3020 apparatus. Samples were degassed at 150 °C overnight in vacuum before nitrogen adsorption was measured.

2.5 X-ray absorption spectroscopy

Extended X-ray absorption fine structure (EXAFS) was measured to probe the short-range order and structure around the Ta atoms. The X-ray absorption spectra were recorded in transmission mode at the Brazilian Synchrotron Light Laboratory (LNLS) at the XAFS1 beamline (proposal XAFS1-12826). The samples were treated at different temperatures and times and then analysed with *ex situ* EXAFS measurements at room temperature. The spectra were collected at the Ta L_3 edge (9881 eV) using a channel-cut Si (111) crystal and three ionization chambers. To calibrate the measurements, a Ta foil was used in the third ionization chamber. EXAFS data were analysed in accordance with the standard procedure for data reduction, using ATHENA and ARTEMIS code from the IFEFFIT software package.[37] FEFF 8.0 was used to obtain the phase shift and amplitudes.[38] The EXAFS signal $\chi(k)$ was extracted and Fourier transformed (FT) using a Kaiser–Bessel window with a k-range from 2.6 to 11.1 $Å^{-1}$ (Δk-range of 8.5 $Å^{-1}$).

3 Results

3.1 Ta_2O_5 NTs formation

Ta_2O_5 NTs were obtained after the Ta metal was anodized for 20 min in H_2SO_4-based electrolytes at two temperatures:

20 and 50 °C.[34] The Ta_2O_5 NTs prepared at 20 °C were well-adhered to the Ta substrate, while the NTs produced at 50 °C were detached from the substrate to form Ta_2O_5 freestanding NTs.[34] The NTs formed at these two electrolyte temperatures, 20 and 50 °C, were 2.0 and 4.3 μm long, respectively. For more details, the reader is encouraged to see ref. 34.

3.2 Structural analysis

Crystalline structure of adhered Ta_2O_5 NTs. Fig. 1 shows a comparison of the XRD patterns obtained for the Ta_2O_5 NTs after different processes: as-anodized NTs and adhered NTs, bare Ta substrate and only freestanding Ta_2O_5 NTs, after heat treatment at 550 °C. The XRD patterns of the adhered as-prepared NTs (Fig. 1a) showed only the metallic phase of Ta (JPCDS file 4-788), which suggests that the as-prepared Ta_2O_5 NTs were amorphous. However, after annealing at 550 °C, the adhered Ta_2O_5 NTs diffraction pattern presented a crystalline phase that was identified as orthorhombic (JPCDS file 25-922) by the agreement of the diffraction peaks (Fig. 1b).

To investigate whether this orthorhombic phase is due to the crystallization of the NTs, and not substrate oxidation, a bare Ta foil was annealed at 550 °C. The diffraction patterns were the same as those observed for the adhered NTs (Fig. 1c). However, at these anodization conditions (50 °C), the NTs were removed from the metallic substrate with only a slight stream of distilled water. The freestanding Ta_2O_5 NTs membranes were submitted to the same annealing conditions (550 °C for 30 min), and the XRD results showed amorphous characteristics (Fig. 1d).

Crystalline structure of freestanding Ta_2O_5 NTs. To study the crystallization of the freestanding NTs, the Ta_2O_5 membranes were annealed at 800 °C for various times and at 900 and 1000 °C for 30 min. The XRD pattern of the sample treated at 800 °C for 30 min showed good agreement with the orthorhombic phase (JPCDS file 25-922), Fig. 2. However, large amorphous content still existed in the NTs, indicating that some NTs still were amorphous[34] or small grains of the orthorhombic phase were distributed in an amorphous matrix.[34] A further increase in the annealing time or temperature greatly decreased the amorphous content, as can be seen in Fig. 2 and Fig. S1.† Table 1 shows the crystallinity degree (X_c) calculated with the area ratio method.[36,39] X_c increased from 11% to 68% when the crystallization time at 800 °C increased from 30 min to 600 min and from 11% to 63% when the heat treatment temperature was raised from 800 to 1000 °C. Moreover, to investigate the effects on the main grain size, Rietveld refinements were performed (Fig. 2 and Fig. S1†). The results are presented in Table 1. The refinements start parameters for Ta_2O_5 included the space group *P2mm* by using the CIF information card (no. 9112). As shown in Table 1, the refined interatomic Ta–O distances are characteristic of TaO_6 octahedral and TaO_7 pentagonal bipyramid units and are consistent with results reported in the literature.[40] The fit quality was available by the R and χ^2 factors, which are in good agreement with the expected values.[41] The local structure of amorphous and crystalline Ta_2O_5 NTs was investigated with EXAFS, and details are presented.

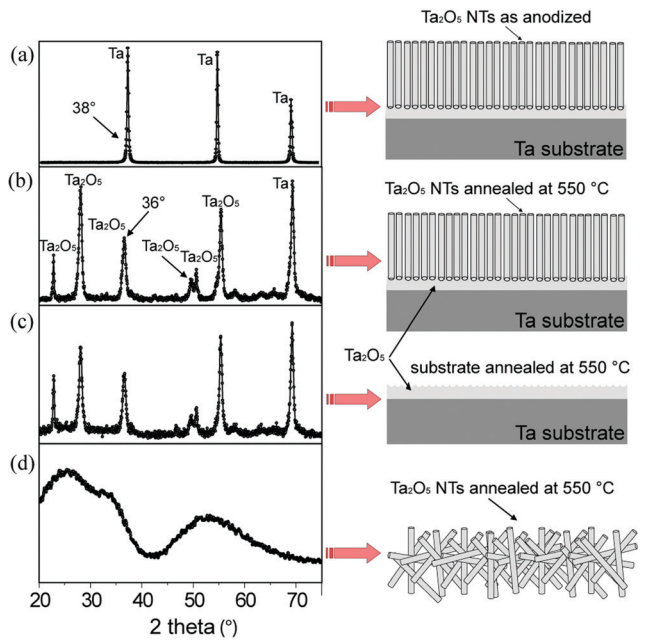

Fig. 1 XRD patterns of various samples prepared with anodization at 20 °C. (a) Adhered Ta_2O_5 NTs as-prepared, (b) adhered Ta_2O_5 NTs annealed at 550 °C for 30 min, (c) Ta metal substrate annealed at 550 °C for 30 min and (d) freestanding Ta_2O_5 NTs heated at 550 °C for 30 min.

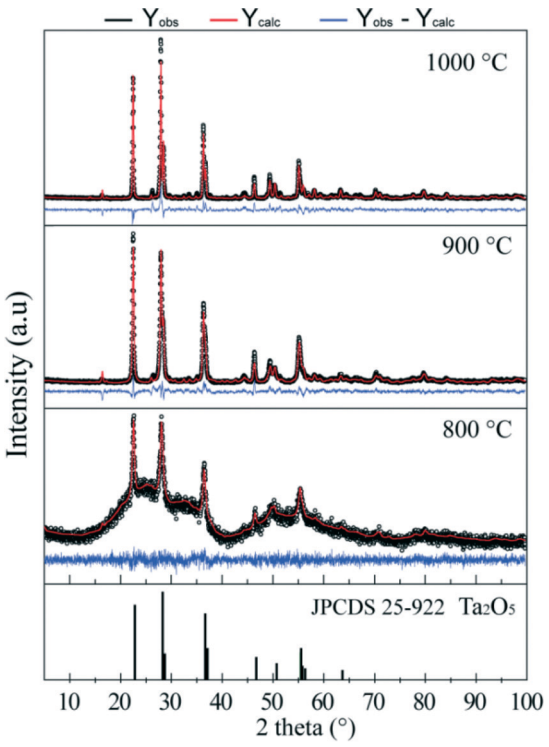

Fig. 2 Rietveld refinement for freestanding Ta_2O_5 NTs heat treated at 800, 900 and 1000 °C for 30 min each.

Table 1 Rietveld refinement data for the Ta_2O_5 NTs sample annealed at various temperatures and for various times

T (°C)	800					900	1000
t (min)	30	60	120	300	600	30	30
Ta–O (Å)	2.07	2.06	2.06	2.07	2.07	2.06	2.07
R_E	6.55	4.81	6.09	6.17	6.15	6.60	6.67
R_p	5.13	5.69	6.07	7.01	7.43	8.34	12.00
R_{wp}	6.60	7.39	8.09	9.23	9.88	11.0	16.50
χ^2	1.01	2.36	1.77	2.24	2.58	2.78	5.94
V (Å^3)	968.7	970.2	969.5	969.8	970.4	971.8	971.7
Density (g cm^{-3})	8.32	8.36	8.33	8.31	8.30	8.31	8.33
Size (nm)	15.4	15.5	25.0	26.0	32.0	31.9	52.4
$\varepsilon \times 10^{-4}$ (%)	24.82	42.12	47.11	39.46	35.86	19.28	19.35
X_c (%)	11 (ref. 34)	34 (ref. 34)	40	53	68	54	63

In Table 1, the average grain size of the Ta_2O_5 crystallites increases at higher temperatures. The crystal size increased from 15.4 nm to 52.4 nm when the heat treatment temperature was raised from 800 to 1000 °C. The Rietveld refinement of the set of samples prepared at 800 °C for 60, 120, 300 and 600 min (Fig. S1†), reveals that the average grain size remained constant from 30 to 60 min, about 15 nm, and after this period slowly increased from 25 to 32 nm by raising the samples annealing time at 800 °C from 120 to 600 min, Table 1.

In addition to the grain size and X_c, information about the microstrain (ε) through Rietveld refinements was obtained, Table 1. The increase in annealing time had an interesting behaviour over the ε value. The microstrain initially increased from 24.82 × 10^{-4} to 47.11 × 10^{-4}% when the annealing time increased from 30 min to 120 min at 800 °C. Extending the sample exposure to heat to 600 min gradually diminished the strain to 35.86 × 10^{-4}%. Moreover, as expected, the increase in the annealing temperature greatly relaxed the crystalline microstrain, Table 1, which attained a minimum value of approximately 19 × 10^{-4}% at 1000 °C.

FESEM analysis of freestanding NTs. The morphological changes in the Ta_2O_5 NTs as a function of temperature and annealing time were monitored with FESEM. As-anodized NTs have continuous smooth walls and are open at the top and closed at the bottom. There were no significant morphological differences between the as-anodized Ta_2O_5 NTs and the NTs annealed up to 800 °C for 30 min (for more details, see ESI S2†). Fig. 3a shows FESEM images of the as-anodized freestanding Ta_2O_5 NTs and those annealed at 800, 900 and 1000 °C. The results show that the freestanding Ta_2O_5 NTs annealed at 800 °C for 30 min did not experience any type of collapse or structure deformation, and maintained the initial nanotubular morphology with 30 nm thick smooth walls.[34] However, the NTs walls begin to deform at 900 °C where small crystals of approximately 30 nm appeared forming holes in the structure. Further increasing the temperature to 1000 °C completely destroyed the tubular structure. At this temperature the NT walls were converted into interconnected nanoparticles with an average size of 100 nm.

Fig. 3b show morphology details as a function of annealing time at 800 °C. Small holes and grains are observed in the tube wall after 60 and 120 min. However, the tubular structure was not yet affected. After 300 min at 800 °C, the NT walls were similar to those of the sample annealed at 900 °C for 30 min (Fig. 3a). Holes and small grains were distributed throughout the structure. Moreover, after 600 min at 800 °C, the morphology was completely lost, and the tubes were converted into interconnected nanoparticles, similarly to NTs annealed at 1000 °C for 30 min.

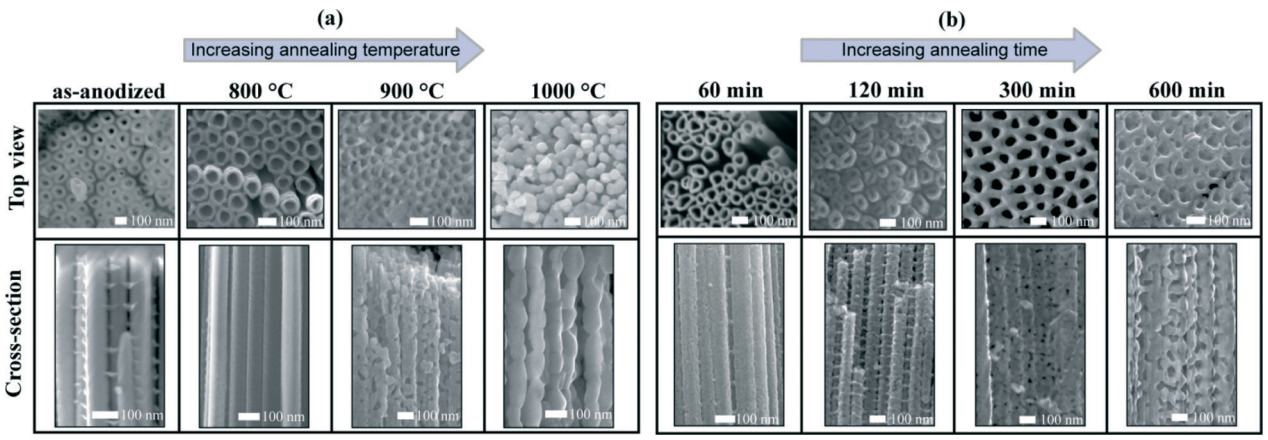

Fig. 3 (a) FESEM images of the top view and cross-section freestanding Ta_2O_5 NTs heated for 30 min at 800, 900 and 1000 °C and (b) the time evolution of heat treatment at 800 °C.

Extended X-ray absorption fine structure. EXAFS experiments were conducted to investigate the local structure of the amorphous and crystalline freestanding Ta_2O_5 NTs membranes. Fig. 4 shows the k^3-weighted EXAFS signal $\chi(k)$ and the corresponding Fourier transforms (FTs) for the set of samples studied. In Fig. 4(a) and (c), the samples subjected to thermal treatments at various temperatures are compared. Fig. 4(b) and (d) show the time evolution for the samples subjected to thermal treatments at a fixed temperature of 800 °C. The $\chi(k)$ curves (Fig. 4(a) and (b)) show clearly changes in the oscillations as the temperature or annealing time increased. For the as-anodized samples annealed at 800 °C for 30 min, there was damping on the $\chi(k)$ oscillations, which is typical for systems with a decreased size and/or low degree of crystallinity. As can be observed, the damping vanished for annealing times longer than 60 min at 800 °C or temperatures higher than 800 °C for 30 min. This observation corroborates previously discussed XRD results and indicates high amorphous content in the as-anodized freestanding Ta_2O_5 NT membranes as well as in those annealed at 800 °C for less than 60 min.

The FT patterns (Fig. 4(c) and (d)) show one well-defined peak at around 1.5 Å (uncorrected for the phase shift), which corresponds to the Ta–O scattering contribution at the coordination shell. The doublet peak around 4 Å in the FT patterns correspond well to the crystallinity of NTs (sample with temperature or annealing time increases).[42] These peaks can be associated with the increase in the crystallinity obtained by XRD measurements. Only single scattering events were considered in the fitting procedure, and the FT was fitted to obtain the local structural information.

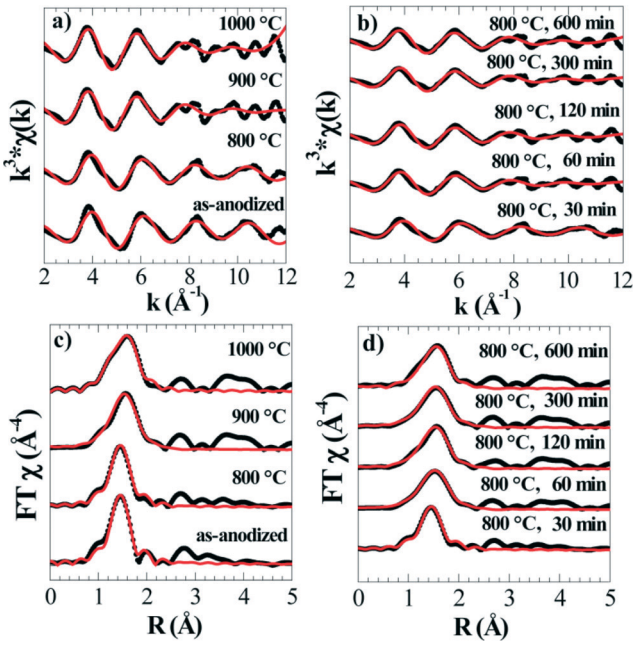

Fig. 4 (a, b) k^3-weighted Ta L_3 EXAFS signal and (c, d) the corresponding Fourier transform magnitude. Red lines represent the best fits obtained.

The red lines represent the best-fitting curve of the data. The unit cell of Ta_2O_5 has 45 atoms grouped in TaO_6 octahedral and pentagonal TaO_7 bipyramid units.[43,44] To simplify the EXAFS analysis, a TaO_6 octahedral unit in the fitting procedure of the coordination shell was considered, and the Ta–O coordination number was allowed to vary up to a maximum value of 7. The procedure of considering TaO_6 octahedral units in the EXAFS analysis has been used in the literature, including recent work.[45] The full data set was adjusted, and excellent agreement between the data and the theoretical structure was found with the low R factor ($\leq$0.03%). The amplitude reduction term (S_0^2) value used was 0.9. The quantitative analysis extracted from the EXAFS data is shown in Table 2.

Due to the low degree of crystallinity, the as-anodized samples and the samples annealed for 30 min at 800 °C were adjusted for cumulant expansion parameters around 10^{-4}. As a result, the Ta–O coordination number increased when annealing was performed above 800 °C or when the annealing time at 800 °C was longer than 30 min. This corresponds to the cases with higher X_c as shown in the Rietveld refinement.

The Ta–O distance shown is the average of the five closest distances of the coordination shell. The Fourier transform comparison presented in Fig. 4(c) shows a slight shift in the first peak position as the annealing temperature increases. However, it is not significant, as shown in the R values in Table 2, considering the error associated with the fitting procedure.

Surface area. To evaluate the surface area of the NTs with annealing, BET was measured. Fig. 5 shows the evolution of the surface area of the as-anodized samples and the samples annealed at 800, 900 and 1000 °C for 30 min, as well as those annealed at 800 °C for 60, 120, 300 and 600 min.

As can be seen, the surface area of the Ta_2O_5 NTs follows the temperature evolution trend: as-anodized < 800 < 900 < 1000 °C. However, the specific surface area dependence on the annealing time at 800 °C first increased to 19.8 $m^2\ g^{-1}$ until 60 min and then started decreasing to around 11 $m^2\ g^{-1}$ after 600 min of annealing.

Table 2 EXAFS fitting parameters

Sample	Scattering	R (Å)[a]	N[b]	σ^2 (10^{-2} Å^2)[c]
As anodized	Ta–O	1.91 ± 0.05	4.7 ± 0.1	1.04 ± 0.04
800 °C	Ta–O	1.92 ± 0.05	4.8 ± 0.1	1.19 ± 0.04
900 °C	Ta–O	2.0 ± 0.1	5.9 ± 0.4	1.2 ± 0.1
1000 °C	Ta–O	2.0 ± 0.2	6.5 ± 0.7	1.3 ± 0.1
60 min	Ta–O	2.0 ± 0.2	6.0 ± 0.5	1.2 ± 0.1
120 min	Ta–O	2.0 ± 0.1	6.1 ± 0.5	1.2 ± 0.1
300 min	Ta–O	2.0 ± 0.2	6.1 ± 0.5	1.2 ± 0.1
600 min	Ta–O	2.0 ± 0.2	5.7 ± 0.6	1.0 ± 0.1

[a] Bond length (Å); [b] coordination numbers (N); [c] Debye–Waller factor (σ^2) for Ta_2O_5 samples.

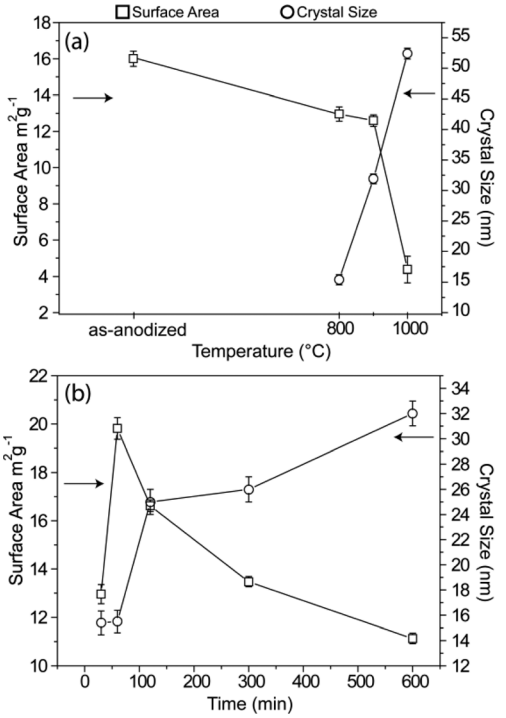

Fig. 5 BET specific surface area evolution of the Ta_2O_5 NTs: (a) as-anodized and annealed at 800, 900 and 1000 °C for 30 min and (b) annealed at 800 °C for 60, 120, 300 and 600 min.

4 Discussion

As published earlier, as-anodized freestanding Ta_2O_5 NTs are amorphous and start to crystallize at 750 °C.[34] Nevertheless, when the tubes were crystallized over the Ta foil from which they were grown, the orthorhombic phase was observed at much lower temperatures, 550 °C, Fig. 1b. However, the crystalline phase observed at this temperature is probably due to the Ta metal oxidation in oxygen-rich atmosphere, Fig. 1c. The crystals formed at the interface of the Ta_2O_5 NTs/Ta metal can also induce tube crystallization, similarly to that observed in the TiO_2 NTs rutile crystallization induced with barrier layer rutile crystals.[20,23,28] This discussion shows that care must be taken to avoid misinterpreting the results of the crystallization process by annealing Ta_2O_5 NTs prepared trough anodization of the Ta metallic substrate.[13,14,20,31,46]

However, the crystallization of freestanding Ta_2O_5 can be investigated without the influence of the substrate oxidation-induced changes in tubes structure and morphology. As can be seen in Tables 1 and 2, the amorphous content dominates the nanotube structure and morphological properties. The crystallinity of the Ta_2O_5 increased by augmenting the temperature and the annealing time, and the mean Ta–O distances are comparable to the bulk crystalline value of 2.06 Å, Table 2 (this value was obtained from the atomic position table in reference data[47]). The mean Ta–O distance in the amorphous material obtained with EXAFS is 1.91 Å, shorter than the value of the crystalline material. High amorphous content, 89%, also dominated the sample annealed for 30 min at 800 °C, showing the same mean distance as the as-anodized sample. However, the EXAFS curve fitting for the NTs with more than 30% orthorhombic phase content gives a Ta–O distance similar to the standard crystalline phase, Table 2. Moreover, as expected, all mean Ta–O distances obtained with Rietveld refinements of the XRD data, Table 1, were similar to the crystalline bulk, about 2.06 Å, since the diffraction signals were due only to the Ta_2O_5 orthorhombic phase.

The coordination number increased as the amorphous content decreased until about 34%, Tables 1 and 2, showing that annealing in oxygen-rich atmosphere increased the coordination number. Considering the uncertainties of EXAFS fittings, the samples annealed for more than 30 min and temperatures higher than 800 °C possess the same coordination number. However, in all samples, except the sample annealed at 1000 °C, the N value is below 7, the theoretical value for the orthorhombic cell of Ta_2O_5. The different values of the theoretical expected to N may be due to the presence of the amorphous phase or to the fact that all Ta atoms were assumed to have octahedral geometry to obtain the approximation of the EXAFS signal.

The increase in NTs crystallinity by increasing the thermal treatment time showed an trend in the microstrain and the morphology of Ta_2O_5, Table 1 and Fig. 3. The microstrain increased to 47×10^{-4} until 120 min of annealing and then suddenly started to diminish. The strain decrease was followed by the appearance of holes in the tube walls, Fig. 3. An additional increase in annealing time to 10 h decreased the tube microstrain even more and completely destroyed the tube walls. The increase in the thermal treatment time obviously increased the crystalline content in the nanotubes, and the Ta_2O_5 grains grew. However, in the case of the Ta_2O_5 NTs, the crystal diameter was limited to the thickness of the tube walls, considering no preferential orientation and growth of the crystals. The tube walls studied in this article were 30 nm thick,[34] and thus, a maximum size of 30 nm was expected for the oxide crystal. Moreover, owing to the intrinsic curvature of the tubes, tensile forces should appear when crystals close to the size of the wall thickness are present in the tubes. These tensile forces tend to disrupt the tubular shape to form interconnected nanocrystals. In the present work, the size of the orthorhombic crystals slowly increased until 120 min, but the strain increased dramatically, Table 1. The size of the crystals formed until 120 min of annealing at 800 °C was 25 nm, less than 30 nm. However, due to the curvature of the tubes, the intercrystal tension doubled, making the tubular structure collapse. As can be seen in Table 1, after 300 min of annealing at 800 °C, the crystals further increased to 26 nm, and the microtension diminished because holes formed in the tube walls, Fig. 3b. Annealing for longer periods, 600 min, further increased the crystal size to 32 nm and decreased the amorphous content and the microstrain due to the complete collapse of the NTs. Similar reasoning can be done for the increase in the thermal treatment temperature. However, the strain evolution in the

temperature variation study was not followed. The samples annealed at 900 °C already had broken walls, Fig. 3a, and the microstrain was much lower than all NTs treated at 800 °C. Moreover, the crystal at 900 °C was 31.9 nm, bigger than possible with tubes with 30 nm-thick walls. The collapse of the tubes observed for annealing at 1000 °C was even more drastic. Obviously, the strain and amorphous content were the lowest found in the work.

The specific area results can be ascribed to the coalescence, collapse and retention of the macroporous structure after crystallization of the NT walls, which is in good agreement with FESEM images and crystal growth from XRD and Rietveld refinements. Increasing the annealing temperature made the crystals grow, which deformed the NT walls and reduced the surface area. However, for the 60 min thermal treatments at 800 °C, the surface area increased. This increase is attributed to the formation of crystallites around 15 nm on the NT walls resulting in microporous formation, as shown in the FESEM image.

The findings described herein bring up an important question. Is it possible to obtain low-defective and high-crystalline Ta_2O_5 NTs? The present work shows that it is just possible to obtain low-crystallinity NTs with an annealing procedure in conventional muffle furnaces. Even when the tubular morphology is completely lost, at 1000 °C, there is almost 40% amorphous Ta_2O_5. In fact, crystallization of the orthorhombic tantalum(v) oxide seems difficult, since its unit cell has 45 atoms, 12 Ta and 33 O, and the several Ta centers possess different coordination, (octahedral, pentagonal bipyramid and hexagonal bipyramid) hampering the atom accommodation inside the unit cell. Moreover, the minimum size of a Ta_2O_5 crystal has to be bigger than 4 nm, since the orthorhombic unit cell has a *b* parameter of 40.07 Å. Thus, the thin walls of the NTs can barely stand the smallest Ta_2O_5 crystal, preventing crystallization of the nanotubes and enhancing the internal stress.

Conclusions

Studies on the crystallization of adhered and freestanding Ta_2O_5 NTs have shown that care must be taken when interpreting the crystallization behaviour of NT arrays obtained by anodizing metal foils. Freestanding Ta_2O_5 NTs are amorphous until 800 °C, and the crystalline phase observed at 550 °C in the NTs over Ta foil is due to metal oxidation, not NT crystallization. This is not the first example of the influence of the interface of metal/oxide NTs on crystallization of the oxide, since TiO_2 anatase to rutile was described earlier. Moreover, the combination of XRD, XAS and FESEM is a powerful methodology for explaining the changes in the structural and morphological properties of Ta_2O_5 NTs. The coordination number, microstrain and morphological changes are all related to the amorphous content and the crystal size of the oxide. The coordination number increased as the crystalline content increased. However, as the amorphous content decreased and the crystals subsequently increased in size, the intercrystal microstrain increased, due to the small size of the tube wall. Moreover, the high strain induced a break in the tubular structure to diminish the tensile forces formed, as observed in the collapse of the tubes observed for annealing above 900 °C and 120 min of treatment at 800 °C. The trends and findings of the present work can help to develop future strategies for preparing high-crystalline semiconductor NTs with a low concentration of defects.

Acknowledgements

The authors acknowledge the Brazilian Synchrotron Light Laboratory (LNLS) for XAFS1 experimental facilities (proposal XAFS1-12826); LNNano for FESEM microscope (proposals SEM-FEG 13057). The authors also thank the Brazilian funding agencies CAPES, CNPq and FAPERGS and ANEEL-CEEE GT under process no. 9945481.

References

1 S. Barth, F. Hernandez-Ramirez, J. D. Holmes and A. Romano-Rodriguez, *Prog. Mater. Sci.*, 2010, **55**, 563–627.
2 B. Liu, K. Nakata, S. Liu, M. Sakai, T. Ochiai, T. Murakami, K. Takagi and A. Fujishima, *J. Phys. Chem. C*, 2012, **116**, 7471–7479.
3 I. S. Cho, Z. Chen, A. J. Forman, D. R. Kim, P. M. Rao, T. F. Jaramillo and X. Zheng, *Nano Lett.*, 2011, **11**, 4978–4984.
4 J. Giblin and M. Kuno, *J. Phys. Chem. Lett.*, 2010, **1**, 3340–3348.
5 T. Zhai, L. Li, Y. Ma, M. Liao, X. Wang, X. Fang, J. Yao, Y. Bando and D. Golberg, *Chem. Soc. Rev.*, 2011, **40**, 2986–3004.
6 L. Wei and M. L. Charles, *J. Phys. D: Appl. Phys.*, 2006, **39**, R387.
7 I. Paramasivam, H. Jha, N. Liu and P. Schmuki, *Small*, 2012, **8**, 3073–3103.
8 J. M. Macak, M. Zlamal, J. Krysa and P. Schmuki, *Small*, 2007, **3**, 300–304.
9 J. R. Jennings, A. Ghicov, L. M. Peter, P. Schmuki and A. B. Walker, *J. Am. Chem. Soc.*, 2008, **130**, 13364–13372.
10 P. Roy, D. Kim, K. Lee, E. Spiecker and P. Schmuki, *Nanoscale*, 2010, **2**, 45–59.
11 K. Zhu and A. J. Frank, *MRS Bull.*, 2011, **36**, 446–452.
12 D. Gong, C. A. Grimes, O. K. Varghese, W. C. Hu, R. S. Singh, Z. Chen and E. C. Dickey, *J. Mater. Res.*, 2001, **16**, 3331–3334.
13 J. E. Barton, C. L. Stender, P. Li and T. W. Odom, *J. Mater. Chem.*, 2009, **19**, 4896–4898.
14 N. K. Allam, X. J. Feng and C. A. Grimes, *Chem. Mater.*, 2008, **20**, 6477–6481.
15 R. R. Rangaraju, K. S. Raja, A. Panday and M. Misra, *Electrochim. Acta*, 2010, **55**, 785–793.
16 D. Fang, K. L. Huang, Z. P. Luo, Y. Wang, S. Q. Liu and Q. G. Zhang, *J. Mater. Chem.*, 2011, **21**, 4989–4994.

17 J. M. Macak, H. Tsuchiya, L. Taveira, S. Aldabergerova and P. Schmuki, *Angew. Chem., Int. Ed.*, 2005, **44**, 7463–7465.
18 J. M. Macák, H. Tsuchiya and P. Schmuki, *Angew. Chem., Int. Ed.*, 2005, **44**, 2100–2102.
19 H. Wender, A. F. Feil, L. B. Diaz, C. S. Ribeiro, G. J. Machado, P. Migowski, D. E. Weibel, J. Dupont and S. R. Teixeira, *ACS Appl. Mater. Interfaces*, 2011, **3**, 1359–1365.
20 J. Yu and B. Wang, *Appl. Catal., B*, 2010, **94**, 295–302.
21 T. J. LaTempa, X. J. Feng, M. Paulose and C. A. Grimes, *J. Phys. Chem. C*, 2009, **113**, 16293–16298.
22 J. Z. Xixin Wang, X. Hou, Q. He and C. Tang, *J. Nanomater.*, 2012, **2012**, 409541.
23 K. Zhu, N. R. Neale, A. F. Halverson, J. Y. Kim and A. J. Frank, *J. Phys. Chem. C*, 2010, **114**, 13433–13441.
24 K. Zhu, N. R. Neale, A. Miedaner and A. J. Frank, *Nano Lett.*, 2006, **7**, 69–74.
25 C. Richter and C. A. Schmuttenmaer, *Nat. Nanotechnol.*, 2010, **5**, 769–772.
26 M. A. Henderson, *Surf. Sci. Rep.*, 2011, **66**, 185–297.
27 V. K. Mahajan, M. Misra, K. S. Raja and S. K. Mohapatra, *J. Phys. D: Appl. Phys.*, 2008, **41**, 125307.
28 D. Fang, Z. Luo, K. Huang and D. C. Lagoudas, *Appl. Surf. Sci.*, 2011, **257**, 6451–6461.
29 Y. Sun, K. Yan, G. Wang, W. Guo and T. Ma, *J. Phys. Chem. C*, 2011, **115**, 12844–12849.
30 B. Yang, C. K. Ng, M. K. Fung, C. C. Ling, A. B. Djurisic and S. Fung, *Mater. Chem. Phys.*, 2011, **130**, 1227–1231.
31 Y. Yang, X. H. Wang and L. T. Li, *J. Am. Ceram. Soc.*, 2008, **91**, 632–635.
32 H. A. El-Sayed and V. I. Birss, *Nanoscale*, 2010, **2**, 793–798.
33 H. A. El-Sayed and V. I. Birss, *Nano Lett.*, 2009, **9**, 1350–1355.
34 R. V. Gonçalves, P. Migowski, H. Wender, D. Eberhardt, D. E. Weibel, F. V. C. Sonaglio, M. J. M. Zapata, J. Dupont, A. F. Feil and S. R. Teixeira, *J. Phys. Chem. C*, 2012, **116**, 14022–14030.
35 J. Rodriguezcarvajal, *Phys. B*, 1993, **192**, 55–69.
36 P. Allia, M. Baricco, P. Tiberto and F. Vinai, *J. Appl. Phys.*, 1993, **74**, 3137–3143.
37 M. Newville, *Synchrotron Radiat.*, 2001, **8**, 322–324.
38 S. I. Zabinsky, J. J. Rehr, A. Ankudinov, R. C. Albers and M. J. Eller, *Phys. Rev. B: Condens. Matter Mater. Phys.*, 1995, **52**, 2995–3009.
39 A. G. Yavuz, A. Uygun and H. K. Can, *Carbohydr. Res.*, 2011, **346**, 2063–2069.
40 X. Q. Liu, X. D. Han, Z. Zhang, L. F. Ji and Y. J. Jiang, *Acta Mater.*, 2007, **55**, 2385–2396.
41 B. H. Toby, *Powder Diffr.*, 2006, **21**, 67–70.
42 D. Lutzenkirchen-Hecht and R. Frahm, *Synchrotron Radiat.*, 2001, **8**, 478–480.
43 J. Ribeiro, G. Tremiliosi-Filho, P. Olivi and A. R. de Andrade, *Mater. Chem. Phys.*, 2011, **125**, 449–460.
44 H. Sawada and K. Kawakami, *J. Appl. Phys.*, 1999, **86**, 956–959.
45 A. Korovina, Y. Garsany, A. Epshteyn, A. P. Purdy, K. More, K. E. Swider-Lyons and D. E. Ramaker, *J. Phys. Chem. C*, 2012, **116**, 18175–18183.
46 O. K. Varghese, D. W. Gong, M. Paulose, C. A. Grimes and E. C. Dickey, *J. Mater. Res.*, 2003, **18**, 156–165.
47 N. C. Stephenson and R. S. Roth, *Acta Crystallogr., Sect. B: Struct. Crystallogr. Cryst. Chem.*, 1971, **27**, 1037–1044.

